Ceramics International 51 (2025) 24859–24867

Contents lists available at ScienceDirect

Ceramics International

journal homepage: www.elsevier.com/locate/ceramint

Design and performance of SiOC foam-silica aerogel composites for hot and cold thermal management applications

Oyku Icin, Cekdar Vakifahmetoglu *

Department of Materials Science and Engineering, İzmir Institute of Technology, 35433, İzmir, Turkey

ARTICLE INFO

Handling Editor: Dr P. Vincenzini

Keywords:
SiOC
Silica
Aerogels
Foam
Composite
Cold insulation
Hot insulation

ABSTRACT

This study focuses on the fabrication of monolithic preceramic polymer-derived ceramic (SiOC) foam-silica aerogel composites by filling the open cells of ceramic foam with a silica aerogel solution using the sol-gel technique. The effects of different drying techniques (ambient pressure vs CO_2 supercritical drying) and surface modification agents, including trimethylchlorosilane (TMCS) and hexamethyldisilazane (HMDZ), are comprehensively investigated. These factors are analyzed for their influence on the composites' morphology, porosity, chemical structure, and thermal insulation performance. The drying technique and surface modification agents are found to play a critical role in achieving a high filling ratio of silica aerogel within the composites. Pure silica aerogels exhibit specific surface areas (SSAs) reaching ~1120 $m^2.g^{-1}$, while the SiOC foam-silica aerogel composites demonstrate SSAs of 385–440 $m^2.g^{-1}$. Nearly all samples achieve a total porosity of ~93 vol%. Surface modification effectively tailors the surface properties, imparting hydrophobicity with a water contact angle of 133°. Thermal conductivity at room temperature ranges between 38 and 43 $mW{\cdot}m^{-1}{\cdot}K^{-1}$. The potential applications of these SiOC foam-silica aerogel composites as thermal insulators are assessed under extreme thermal conditions. For instance, a 14 mm thick composite has a temperature of -27 °C when subjected to a cold source at -78 °C. Instead, when exposed directly to a butane flame (~1200 °C), the backside of the composite recorded only ~57 °C.

1. Introduction

Aerogels are innovative porous materials characterized by a 3-dimensional network of ultrafine interconnected particles, nanoscale pore sizes (<100 nm) with high porosity (typically exceeding 80 vol%) [1,2]. Their unique properties such as low density, high specific surface area (SSA), and low thermal conductivity (at room temperature, RT), make them ideal candidates for a wide range of applications, including insulation, fire retardants, aerospace components (e.g., particle capture), energy absorber, capacitors, catalysts, and adsorption of oils, dyes, metals, etc. [3–5].

Among the various types, silica-based aerogels—typically synthesized through a sol-gel process—have been the most extensively studied since their discovery in the early 1930s [6]. They are prepared in two steps: *i)* sol-gel and *ii)* drying using a suitable, almost shrinkage-free drying procedure under ambient pressure conditions via surface modifications or CO_2 supercritical drying [7,8]. The resulting aerogels are typically highly mesoporous with low densities (ranging from 0.03 to 0.3 $g.cm^{-3}$) possessing substantial SSA values (up to 1000 $m^2.g^{-1}$) and may feature low thermal conductivities (15–50 $mW{\cdot}m^{-1}{\cdot}K^{-1}$) at RT [9–11].

The primary limitation of silica aerogels is their inherent fragility, brittleness, and susceptibility to damage under relatively low-stress levels, which dramatically restricts their application capacity [12–14]. Additionally, fabricating neat monolithic silica aerogels remains challenging [15]. Accordingly several methods have been proposed as a remedy. Among those, the composite strategy has been proposed by filling aerogel into the large cavities of the mother substrate, improving mainly the structural integrity and thus, for example, machinable components can be formed. In this context, most of the studies were based on polymeric foam substrates [16–23]. However, polymeric substrates are only suitable for a limited number of applications, as their stability is highly dependent on the operating conditions. Moreover, the demand for incombustible and non-toxic insulation materials has become increasingly critical across various sectors, including construction and the automotive industry.

Polymer-derived amorphous silicon oxy carbide (SiOC) ceramic foam offers advantages due to greater thermal stability and chemical

* Corresponding author.
E-mail addresses: cekdarvakifahmetoglu@iyte.edu.tr, cvahmetoglu@gmail.com (C. Vakifahmetoglu).

https://doi.org/10.1016/j.ceramint.2025.03.167
Received 13 January 2025; Received in revised form 14 February 2025; Accepted 10 March 2025
Available online 10 March 2025

durability compared to those of polymeric substrates used similarly [24–26]. In addition, SiOC is chemically closer to silica, implying a stronger bonding [27]. Consequently, this study focused initially on filling the cells of SiOC foams with silica aerogels for which the final pore sizes were deliberately tailored with different drying methods (ambient pressure and CO_2 supercritical) and surface modifications. Following the processing, the formed monoliths were targeted and evaluated for their effectiveness in thermal management applications, specifically in extreme hot and cold environments.

2. Experimental procedure

2.1. Materials

A commercial polymethyl-silsesquioxane preceramic polymer was obtained from Wacker GmbH (MK Belsil, Wacker GmbH, Burghausen, Germany). Acetone (99.5 %, Tekkim, CAS: 67-64-1, Turkiye), Ethanol (EtOH; absolute 99.5 %, Tekkim, CAS: 64-17-5, Turkiye), and n-hexane (extra pure >96 %, Isolab, CAS: 110-54-3) were used as the solvents. 90 PPI PU foams with an open cell structure (A.R.E., Milan, Italy) were used as a template for preparing SiOC foams. For silica aerogel, sol-gel chemicals were Tetraethyl orthosilicate (TEOS, reagent grade 98 %, Sigma-Aldrich, CAS: 78-10-4) as silica source, Hydrochloric acid (HCl) solution (1 M, Titripur®, Merck, CAS: 7647-01-0), Ammonia solution (NH_4OH; 25 %, Isolab, CAS: 1336-21-6) as acid-base catalysts, and deionized water (DIW). Additionally, Chlorotrimethylsilane (TMCS, 98 %, Thermo Scientific Chemicals, CAS: 75-77-4) and 1,1,1,3,3,3-Hexamethyldisilazane (HMDZ, 98 %, Thermo Scientific Chemicals, CAS: 999-97-3) were selected as surface modification agents. Also, CO_2 (99.5 %) was used for the supercritical drying process.

2.2. SiOC foam production

Preceramic resin-derived SiOC foams were produced using the replica technique with flexible PU foams (90 PPI) as the template. The recipe for the preparation involved a PU/PMS/acetone weight ratio of 1:2:20. Following a previously published procedure [28], PU foams were initially cut into discs (~35 mm and a thickness of ~5 mm). The preceramic resin was dissolved in acetone, and the solution was stirred at 500 rpm at RT for 10 min to ensure complete dissolution. The foams were then impregnated with the solution in glass Petri dishes. After allowing the impregnated foams to dry for 1 h, they were subjected to a curing process at 200 °C for 6 h to stabilize the resin within the foam structure. Finally, polymeric foams were pyrolyzed under Argon (Ar) flow (200 mL min^{-1}) at 1000 °C in an alumina tube furnace (PROTERM PTF 16/75/450, Ankara, Turkey) with a heating rate of 2 °C.min^{-1} for 2 h (dwell time), yielding SiOC ceramic foams.

2.3. Production of silica aerogel-filled SiOC foam composites

Silica gels based on TEOS were prepared through a two-step acid-base catalyzed sol-gel process. The overall molar ratio of TEOS:EtOH:water:HCl:NH_4OH was kept constant at 1:9.3:3.7:1.04×10^{-4}:8.3×10^{-3}, respectively. Initially, the silica precursor (0.025 mol of TEOS) was dissolved in 2.18 mL of EtOH, and 2.17 mL of an EtOH/1M HCl solution stock solution (109.24 mL/260 μL). Next, 0.46 mL of DI water was added to form a sol, and the solution was stirred at 250 rpm for 90 min. Subsequently, 9.2 mL of EtOH and 1.2 mL of DI water/25 % NH_4OH stock solution (168 g/1 g) were added, with stirring continuing at 250 rpm for 30 min.

For the aerogel-filled foam composite synthesis, the sol was poured into Teflon molds, fully submerging the SiOC foam. The gelation of the disc shape samples occurred for 24 h at 70 °C. Afterward, a solvent refresh was carried out using excess EtOH (twice/day for 2 days). The solvent exchange was conducted using mixtures of EtOH and hexane (1:3, 1:1, and 3:1 vol%, respectively), and pure hexane (twice/day for 2 days) for samples to be subjected to surface modification. Wet gels were treated with a 6 vol% solution of silylation agents (TMCS and HMDZ, with a silylation agents/TEOS molar ratio of 1:1) in hexane at RT for 24 h. Residual surface modification reagents were rinsed off with hexane. Finally, modified samples were dried in the oven, following a temperature sequence of 65 °C for 3 h, 80 °C for 1 h, 120 °C for 1 h, and 150 °C for 1 h. A supercritical dried sample was also produced using CO_2 supercritical drying (SCD) at 200 bar and 50 °C for 2 h.

Foam-aerogel composite samples were coded as $Foam_{SiOC}$-$Aerogel_{SiO2\text{-}X}$ implies a composite material composed of a SiOC foam ($Foam_{SiOC}$) combined with silica aerogel ($Aerogel_{SiO2\text{-}X}$), 'x' indicating the specific treatment or modification applied (e.g., 'SCD' for supercritical drying or 'TMCS Mod./HMDZ Mod.' for trimethylchlorosilane/hexamethyldisilazane modification.

2.4. Characterization

The fractured surface morphology of the samples was investigated using scanning electron microscopy (SEM, FEI Quanta 250 FEG). Before SEM analysis, the samples were coated with a thin gold layer (approximately 10 nm) using a sputter coater (Emitech K550X, Quorum Technologies).

Fourier transform infrared (FT-IR) spectra were recorded using a Spectrum Two FT-IR spectrometer (PerkinElmer) with a UATR accessory. The measurements were taken in transmission mode over the range of 400–4000 cm^{-1}, with 20 scans and a resolution of 4 cm^{-1}, to study the structural features of the samples. X-ray diffraction (XRD, Bruker D8 Advance) was performed with Cu Kα radiation over a 2θ range of 10–80°, using a step size of 0.2° and a counting time of 0.1 s per step. The FTIR and XRD data were normalized before plotting.

To assess the thermal stability of $Foam_{SiOC}$ and $Foam_{SiOC}$-$Aerogel_{SiO2}$ composites were analyzed using thermogravimetric analysis (TG/DTA, PerkinElmer Diamond, USA) at a heating rate of 5 °C·min^{-1} under nitrogen (N_2) atmosphere up to 1000 °C.

N_2 sorption analysis was conducted using a Micromeritics 3FLEX Adsorption Analyzer. Before testing, the samples were degassed at 200 °C for 24 h. SSA was calculated using the Brunauer–Emmett–Teller (BET) method, while the pore size distribution was determined using the Barrett–Joyner–Halenda (BJH) method. Wetting behavior was assessed with a Theta Model contact angle (CA) measurement device (KSV-Attension). Contact angle measurements were taken from digital images of 5 μL distilled water droplets placed on the top surface of the samples.

The bulk density measurements were conducted by geometric measurements. The true densities of the samples were calculated by applying the rule of mixture using the following equation: $\rho_{composite} = P\cdot\rho_{foam} + (1\text{-}P)\cdot\rho_{aerogel}$ where ρ_{foam} is the SiOC skeletal density [29] with a value of 2.1 g.cm^{-3}, $\rho_{aerogel}$ is the skeletal density of the silica aerogels [30] (2.2 g.cm^{-3}), and P is the porosity of the samples. The total porosity of composites was subsequently calculated.

Thermal conductivity was measured using a TCi Thermal Conductivity Analyzer (C-Therm Technologies Ltd., Fredericton, Canada) based on the modified transient plane source (MTPS) method. To ensure the reliability of the data, each measurement was repeated ten times, and the mean values, along with standard deviations, were calculated. Additionally, the samples were subjected to controlled heating on a hot plate set to 200 °C, hit with a butane flame gun, and put on dry ice as a cold source, then their surface temperatures were monitored using an infrared thermal imaging camera (FLIR ThermaCAM PM695) to assess temperature distribution and thermal response characteristics.

3. Results & discussion

3.1. Microstructural

The fractured surface SEM images of the neat SiOC foam and aerogel parts of the composites are shown in Fig. S1. The microstructure of SiOC

foam (~96 vol% total porosity) had cell sizes of 517 ± 83 μm and strut thicknesses of 24 ± 5 μm, as shown in Fig. S1a. The higher magnification SEM images (Figs. S1b–d) of the aerogel structures showed a typical aggregation of nanosized or small particles regardless of drying technique or modification agents. However, HMDZ-modified silica aerogel had smaller-sized particles and pores, showing a more compact structure. TMCS-modified and SCD-silica aerogels had larger pores.

The digital photos of the SiO_2 aerogel-filled SiOC foam composite (labeled as $Foam_{SiOC}$-$Aerogel_{SiO2}$) and SEM micrographs (fractured surfaces) are given in Fig. 1a,b,c. The appearance of composites, due to Rayleigh scattering, is a bluish haze [31]. Additionally, the light scattered by the aerogel contrasted sharply with the black SiOC foam background, intensifying the perceived bluish color.

When all sample fracture surfaces SEM micrographs were investigated, it can be seen that the foam cells were almost fully filled for TMCS-modified silica aerogel system ($Foam_{SiOC}$-$Aerogel_{SiO2\text{-}TMCS\ Mod.}$), see Fig. 1b. Instead, in the composites with HMDZ-modified ($Foam_{SiOC}$-$Aerogel_{SiO2\text{-}HMDZ\ Mod.}$; Fig. 1c) and SCD silica aerogel ($Foam_{SiOC}$-$Aerogel_{SiO2\text{-}SCD}$; Fig. 1a), interfacial gaps can be seen between the foam struts and aerogels. Although both composites were synthesized using equal amounts of silylation agents and had similar volumes before drying, the observed differences between the surface-modified composites can be attributed to the greater re-expansion caused by the spring-back effect in TMCS compared to the HMDZ modification system [32]. On the other hand, the $Foam_{SiOC}$-$Aerogel_{SiO2\text{-}SCD}$ composite underwent a small amount of volume shrinkage during the supercritical drying.

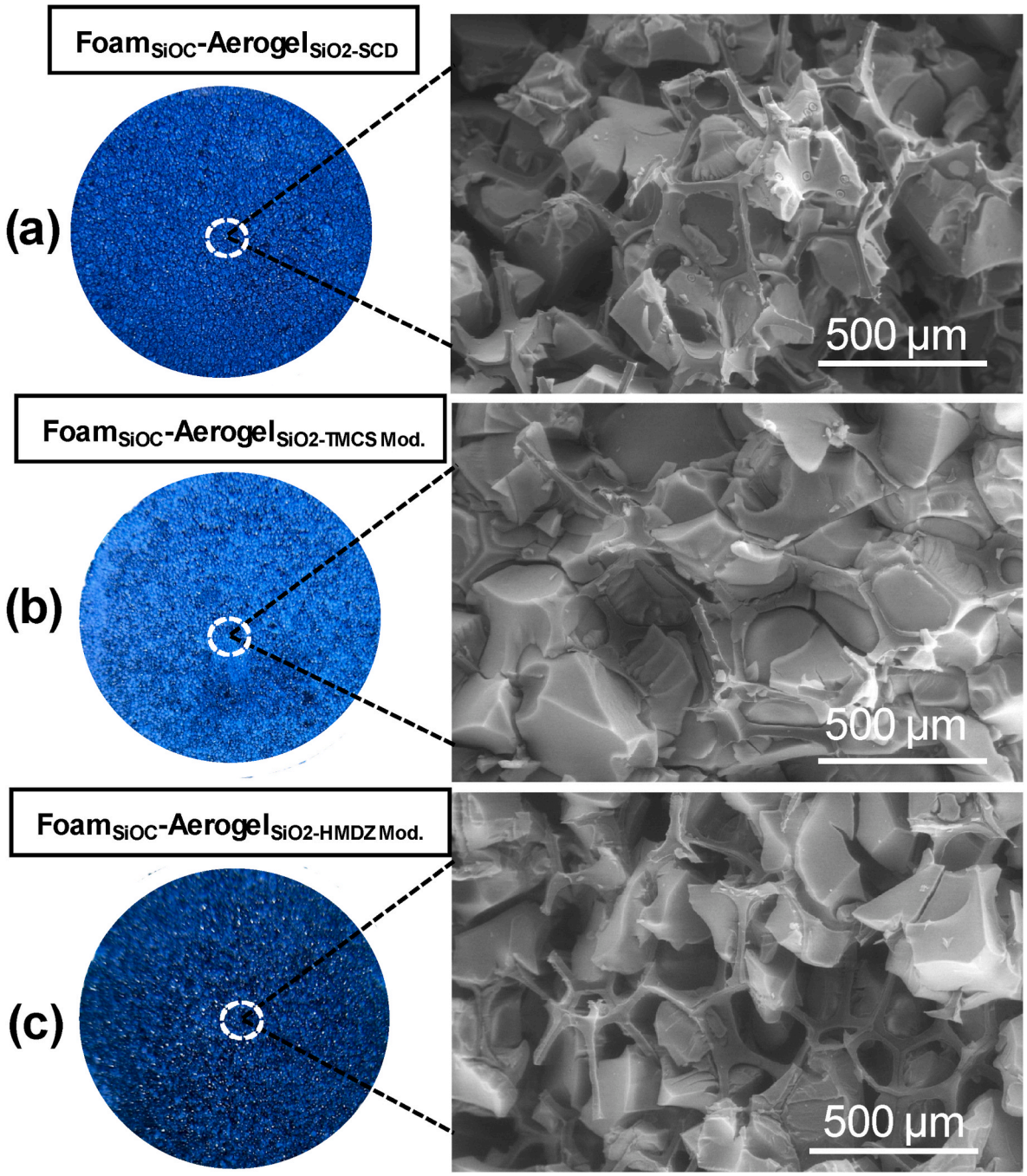

Fig. 1. Digital and SEM (fractured surface) images of SiOC foam-Silica aerogel composites; **(a)** $Foam_{SiOC}$-$Aerogel_{SiO2\text{-}SCD}$, **(b)** $Foam_{SiOC}$-$Aerogel_{SiO2\text{-}TMCS\ Mod}$, and **(c)** $Foam_{SiOC}$-$Aerogel_{SiO2\text{-}HMDZ\ Mod}$.

Due to the characteristic inherent fragility of the investigated system, sample preparation for microstructural analysis may introduce additional cracks, gaps, and cavities, causing further difficulty in obtaining authentic fracture surface images. To illustrate the aerogel distribution, supplementary SEM images of the aerogel-foam composites are also presented in Fig. S2. The overall aerogel coverage of the foam cells was directly influenced by the spring-back efficiency, with a higher spring-back effect leading to greater filling, as previously reported in the literature [16].

The interfacial gaps between the foam substrate and aerogel can lead to increased thermal conductivity, thereby deteriorating the overall thermal insulation performance of the composite [33].

3.2. Structural

The ATR-FTIR spectra of the $Foam_{SiOC}$, $Aerogel_{SiO2}$, and their composites ($Foam_{SiOC}$-$Aerogel_{SiO2}$) are given in Fig. 2a and b. SiOC foam substrate showed the following three characteristic signals. At 417 cm^{-1} the Si−O bond corresponds to Si−O−Si deformation, a signal near 790 cm^{-1} attributed to Si–C and Si–O stretching, and a broad peak around 1050 cm^{-1} associated with Si−O stretching caused by Si−O−Si vibrations within the SiOC network [34]. On the other hand, neat silica aerogels displaced a characteristic Si−O−Si asymmetric stretching vibration at 1070 cm^{-1}, consistent with their silica structure [35]. An in-plane stretching vibration at 965 cm^{-1} and a broad absorption band 3500 cm^{-1}, was observed prominently in the $Aerogel_{SiO2\text{-}SCD}$ sample but was negligible in the modified aerogels, such as $Aerogel_{SiO2\text{-}TMCS\ Mod}$ and $Aerogel_{SiO2\text{-}HMDZ\ Mod}$, likely due to the presence of O−H or Si−OH groups.

Additionally, a symmetric deformation vibration at 1255 cm^{-1} and a stretching vibration at 2980 cm^{-1}, attributed to C−H groups, along with a stretching vibration at 845 cm^{-1} and a peak at 755 cm^{-1}, corresponding to Si−C bonds, were identified in the $Aerogel_{SiO2\text{-}TMCS\ Mod}$ and $Aerogel_{SiO2\text{-}HMDZ\ Mod}$ samples [32]. These results indicate that the disappearance of absorption bands associated with O−H groups, along with the appearance of characteristic bands for alkyl groups, confirms the successful modification of the silica aerogel surface. For SiOC foam-silica aerogel composites, no additional bands were detected beyond those corresponding to the neat SiOC foam and silica aerogel, indicating no significant changes in their spectral features.

Fig. 3 displays the X-ray diffraction patterns of the SiOC foam substrate and SiOC foam-silica aerogel composites. The broad Bragg reflection observed between ~20° and 30° (2θ) indicates the presence of amorphous silica [29,36]. No peaks that can be resolved for a crystalline structure were detected in the SiOC foam substrate or the silica aerogel components of the composites. Thermogravimetric analysis data of the $Foam_{SiOC}$ and $Foam_{SiOC}$-$Aerogel_{SiO2}$ composites are given in Fig. 3b. According to TGA results, no weight loss was observed for the SiOC foam substrate at 1000 °C. In SiOC foam-silica aerogel composites, weight loss was attributed solely to the silica aerogel components, with losses of 8.3 % for $Foam_{SiOC}$-$Aerogel_{SiO2\text{-}SCD}$, 9.7 % for $Foam_{SiOC}$-$Aerogel_{SiO2\text{-}TMCS\ Mod.}$, and 7.8 % for $Foam_{SiOC}$-$Aerogel_{SiO2\text{-}HMDZ\ Mod}$. For the $Foam_{SiOC}$-$Aerogel_{SiO2\text{-}SCD}$ composite, weight loss began around 100 °C, likely due to the evaporation of surface-adsorbed water and subsequent condensation reactions of hydroxyl groups [37]. Between 100 °C and 570 °C, weight loss corresponded to the thermal decomposition of unhydrolyzed ethoxy groups from the TEOS precursor [32]. In contrast, the modified composites exhibited negligible weight loss below 350 °C, indicating minimal adsorbed water. Major weight loss (>400 °C) in all modified samples was linked to the thermal decomposition of surface methyl groups introduced during modification. Literature suggests that the decomposition of methyl groups occurs at intermediate temperatures (between 300 and 500 °C) [38]. Overall, the thermal analysis confirmed that surface-modified silica aerogels are stable up to 350 °C.

3.3. Porosity & surface

Figure S3a and Fig. 4a illustrate the N_2 sorption isotherms of silica aerogels and SiOC foam-silica aerogel composites, respectively. Silica aerogels showed typical type IV hysteresis loops, known for mesoporous materials.

When neat aerogels were investigated, the amount of adsorbed N_2 at high relative pressures (cumulative pore volume) was higher for the SCD (V_{pore} = 2.9 $cm^{-3}.g^{-1}$) and TMCS modified system (V_{pore} = 2.7 $cm^{-3}.g^{-1}$) (Fig. S3a) compared to HMDZ modification (V_{pore} = 1.9 $cm^{-3}.g^{-1}$). Instead, in the composite system (see Fig. 4a), irregular macro-pores formed between the silica aerogel and the pore walls of the SiOC foam. Consequently, the pore volume was smaller than expected. The calculated SSA values of neat aerogels were 1117 $m^2.g^{-1}$ (SCD), 738 $m^2.g^{-1}$ (TMCS), and 737 $m^2.g^{-1}$ (HMDZ) were higher than the composite counterparts such as 440 $m^2.g^{-1}$ ($Foam_{SiOC}$-$Aerogel_{SiO2\text{-}TMCS\ Mod.}$) > 396 $m^2.g^{-1}$ ($Foam_{SiOC}$-$Aerogel_{SiO2\text{-}SCD}$) > 385 $m^2.g^{-1}$ ($Foam_{SiOC}$-$Aerogel_{SiO2\text{-}HMDZ\ Mod.}$). Similar observations in aerogel-based composites highlight the common mechanisms leading to SSA reduction; (i) partial infiltration of aerogel into the substrate, leading to pore structure modification. (ii) increased structural density due to the ceramic framework, reducing the accessible surface area, and (iii) variations in effective aerogel content within different composite structures, affecting SSA

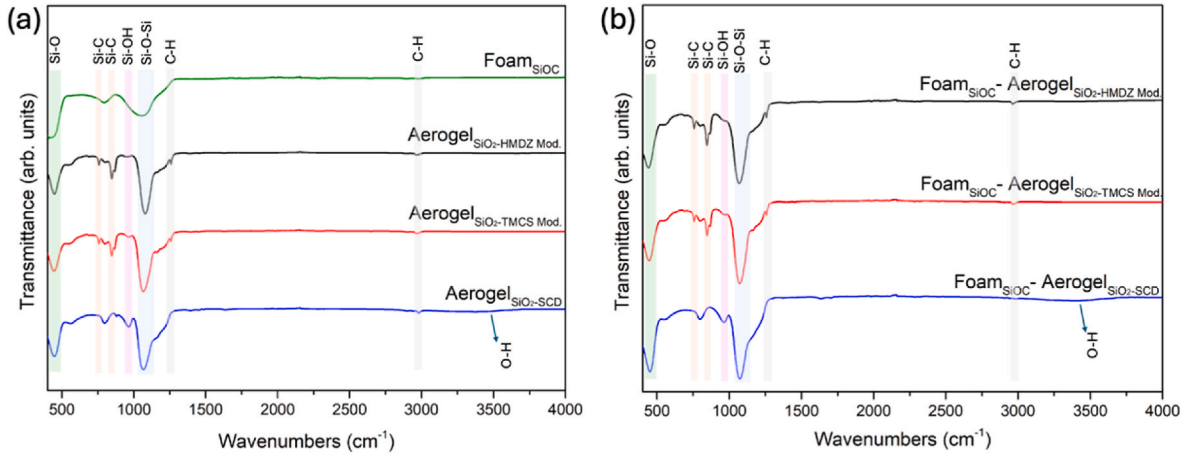

Fig. 2. Normalized ATR-FTIR spectra of **(a)** SiOC foam, neat silica aerogel after CO_2 supercritical drying (SCD), silica aerogel modified with trimethylchlorosilane (TMCS Mod.), and hexamethyldisilazane (HMDZ Mod.) and **(b)** SiOC foam-silica aerogel composite after CO_2 supercritical drying (SCD), modified with trimethylchlorosilane (TMCS Mod.), and hexamethyldisilazane (HMDZ Mod.).

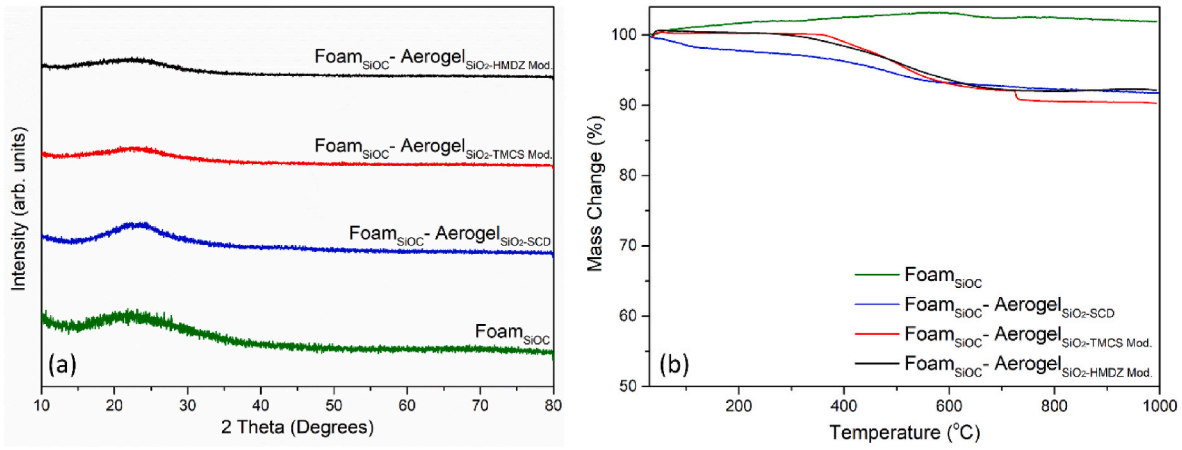

Fig. 3. **(a)** Normalized X-ray diffraction (XRD) patterns, and **(b)** Thermogravimetric analysis (TGA) data (5 °C.min^{-1}; N_2 flow) of SiOC foam substrate and SiOC foam-silica aerogel composite after CO_2 supercritical drying (SCD), modified with trimethylchlorosilane (TMCS Mod.), and hexamethyldisilazane (HMDZ Mod.).

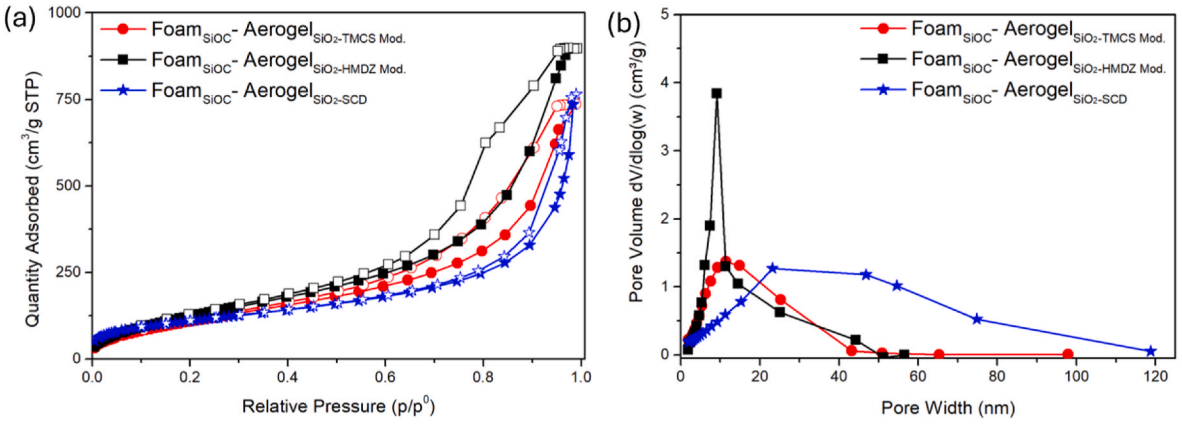

Fig. 4. **(a)** N_2 sorption isotherms of SiOC foam-silica aerogel composites produced either through supercritical drying (SCD) or by surface modification followed by ambient pressure drying, and **(b)** pore size distribution curves.

measurements [25,39].

CO_2 supercritical drying is the typical method for preserving high porosity and specific surface area. This is because it prevents liquid-vapor phase transitions, and induces structural rearrangements leading to additional condensation reactions and network coarsening, which may lower SSA compared to modified-APD composites. Surface modification agents, such as TMCS, in APD enhanced SSA by preventing pore collapse through hydrophobic –Si(CH$_3$)$_3$ groups, reducing capillary stress and promoting spring-back. The shift in pore size distribution toward smaller values in modified aerogels contributes to higher SSA, aligning well with previous findings on SCD-derived samples [40].

Pore size distribution graphs are given for neat silica aerogels in Fig. S3b and their SiOC foam composites in Fig. 4b. The average pore size and volume data are also provided in Table 1. While all systems displayed similar characteristics, the SCD system was distinguished by its broader pore size distribution. The total porosity was determined using the bulk and skeletal densities. Initially, the SiOC foam exhibited a total porosity of ~96 vol%. Upon infiltration with aerogels, the total porosity of the foam-aerogel composites slightly decreased to a range of ~93 vol%.

Contact angle images of SCD (unmodified) and modified silica aerogels (Fig. S4), as well as SiOC foam-silica aerogel composites (Fig. 5), illustrate the transition from hydrophilic to hydrophobic behavior following surface modification. The water droplet contact angle (θ_c) was measured to be 37° for Aerogel$_{SiO2-SCD}$ and 32° for Foam$_{SiOC}$-Aerogel$_{SiO2-SCD}$, indicating a hydrophilic nature. In contrast, modification increased it to over 130° for all treated samples (as shown in Figures S4b,c and Fig. 5b,c by changing silanol groups on the silica surface with trimethylsilyl groups [41] Notably, the TMCS-modified silica aerogel demonstrated superhydrophobicity [38] with a contact angle of 156° (Fig. S4b), which decreased to 131° for Foam$_{SiOC}$-Aerogel$_{SiO2-TMCS Mod.}$ composite. This reduction might be attributed to the hydrophilic nature of the SiOC foam substrate. Although HMDZ and TMCS modification

Table 1
Structural properties of neat SiOC foam and SiOC foam–silica aerogel composites. Bulk densities were determined using geometrical measurements, while the specific surface area (SSA), cumulative pore volume, and average pore size were analyzed via N_2 sorption measurements.

Sample Codes	Bulk Density (g. cm^{-3})	Porosity (vol%)	SSA (m^2.g^{-1})	Pore Vol. (cm^3.g^{-1})	Avg. Pore size (nm)
Foam$_{SiOC}$	0.09	95.6	1.2	–	–
Foam$_{SiOC}$-Aerogel$_{SiO2-SCD}$	0.12	94.5	396	1.1	12.9
Foam$_{SiOC}$-Aerogel$_{SiO2-TMCS Mod.}$	0.14	93.4	440	1.1	8.5
Foam$_{SiOC}$-Aerogel$_{SiO2-HMDZ Mod.}$	0.14	93.6	385	1.3	8.5

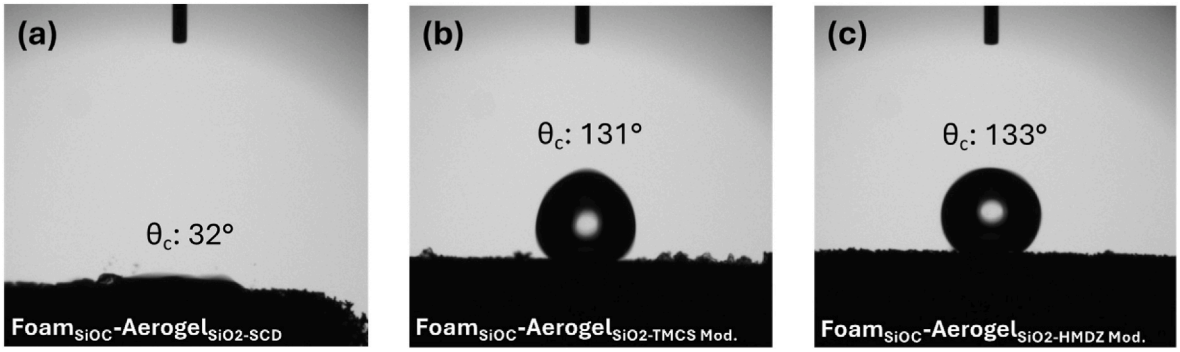

Fig. 5. Digital images demonstrate water droplets placed on the foam-aerogel composites produced through SCD; **(a)** $Foam_{SiOC}$-$Aerogel_{SiO2\text{-}SCD}$, or surface modification followed by ambient pressure drying; **(b)** $Foam_{SiOC}$-$Aerogel_{SiO2\text{-}TMCS\ Mod.}$, and **(c)** $Foam_{SiOC}$-$Aerogel_{SiO2\text{-}HMDZ\ Mod.}$

agents have the same end groups, the latter might lead to higher hydrophobicities because of differences in reactivity [42].

3.4. Thermal insulation

The thermal insulation properties of samples were investigated by measuring the temperature response at three different conditions (on top of a hot source, on dry ice, and under a butane torch hit). Fig. 6a shows the test setup in which the sample was put on a hot plate at 200 °C by recording the surface temperature via a thermal infrared camera. The surface temperature was recorded at 0 s, 15 min, and 30 min, for samples having different thicknesses ranging from 4.7 to 14.1 mm. The detailed thermal infrared images are provided in Figs. S5–S8.

The insulation performance of the samples, each with a thickness of 4.7 mm, is presented in Fig. 6b. The neat SiOC foam reached a temperature of ~76 °C immediately upon heating (at 0 s). In contrast, the surface temperature of the $Foam_{SiOC}$-$Aerogel_{SiO2}$ composites only increased to 46 °C under the same conditions. As the contact time increased, the recorded temperatures rose to 106 °C for the HMDZ-modified composite, 104 °C for the SCD-modified composite, and 95 °C for the TMCS-modified composite. After 15 min, the temperatures stabilized and remained constant, showing no differences between the readings at 15 min and 30 min.

The surface temperature as a function of sample thickness (Fig. 6c) demonstrates that thicker composites (14.1 mm) achieved a more significant temperature difference (ΔT = ~135 °C) between the sample surface (~65 °C) and the hot stage, indicating better thermal insulation performance.

Fig. 6d–g also show the surface temperature variations of the $Foam_{SiOC}$ and $Foam_{SiOC}$-$Aerogel_{SiO2\text{-}TMCS\ Mod.}$ composite (with a thickness of 4.7&14.1 mm) after 30 min of heating, as recorded by an infrared thermal camera.

Room-temperature thermal conductivity measurements conducted via the MTPS method (Fig. 7a) showed the values of 34.8 ± 0.3 $mW{\cdot}m^{-1}{\cdot}K^{-1}$ for SiOC foam, for $Foam_{SiOC}$-$Aerogel_{SiO2\text{-}TMCS\ Mod.}$, 41.5± 0.1 mW m^{-1} K^{-1} for $Foam_{SiOC}$-$Aerogel_{SiO2\text{-}HMDZ\ Mod.}$, and 43.2± 0.2 mW m^{-1} K^{-1} for $Foam_{SiOC}$-$Aerogel_{SiO2\text{-}SCD}$. We aimed to measure the high-temperature thermal conductivity values of composites using the laser flash technique, quantifying thermal diffusivity. However, since the method is actually optimized for opaque materials, we could not get scientifically logical data in our samples [9,43].

To evaluate the high-temperature insulation performance of prepared samples, a butane flame (~1200 °C) was applied to hit a 14 mm-thick neat SiOC foam and foam-aerogel composites for up to 60 s. The experimental setup was illustrated in Fig. 7b, while the backside temperature of the tested samples was shown in Fig. 7c–f and Figs. S9a–b. At 30 s of flame exposure, the backside temperature of the neat $Foam_{SiOC}$ was recorded as 267 °C (Fig. 7c). In contrast, the $Foam_{SiOC}$-$Aerogel_{SiO2\text{-}TMCS\ Mod}$ exhibited a significantly lower backside temperature of 57 °C (Fig. 7e). After turning off the flame at 60 s, the surface temperatures at 120 s were observed as follows: 51.5 °C and 85.8 °C for $Foam_{SiOC}$ (Fig. 7d) and $Foam_{SiOC}$-$Aerogel_{SiO2\text{-}TMCS\ Mod.}$ (Fig. 7f), respectively.

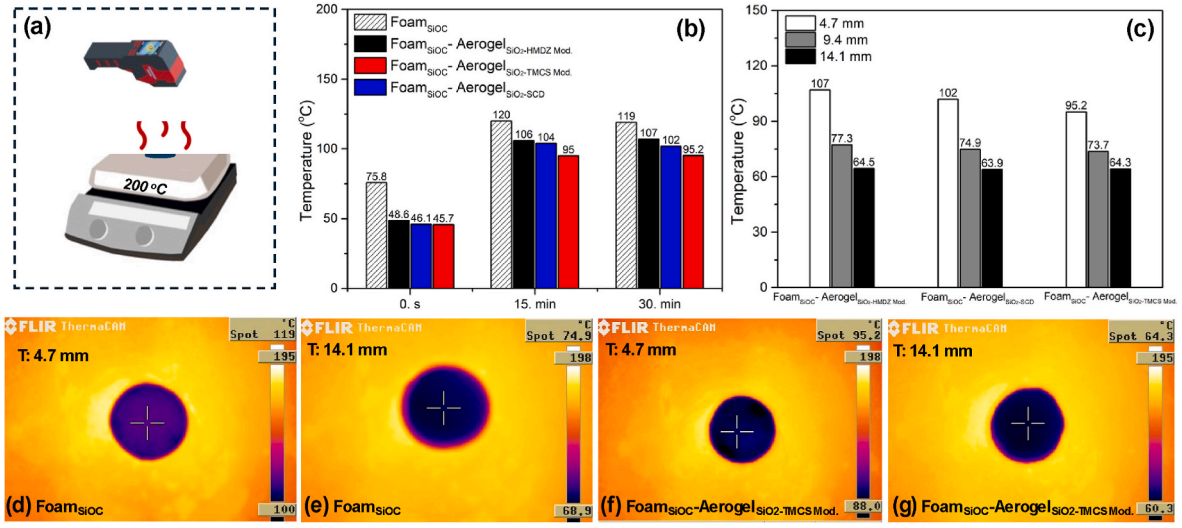

Fig. 6. **(a)** Schematic representation of the hot plate thermal insulation test, **(b)** the relationship between surface temperature of test samples (4.7 mm thickness) and heating time, **(c)** the effect of composite thickness (ranging from 4.7 to 14.1 mm) on thermal insulation performance after 30 min of heating, along with thermal infrared images of $Foam_{SiOC}$ with various thickness; **(d)** 4.7 mm, **(e)** 14.1 mm, and $Foam_{SiOC}$-$Aerogel_{SiO2\text{-}TMCS\ Mod.}$ composite **(f)** 4.7 mm, **(g)** 14.1 mm.

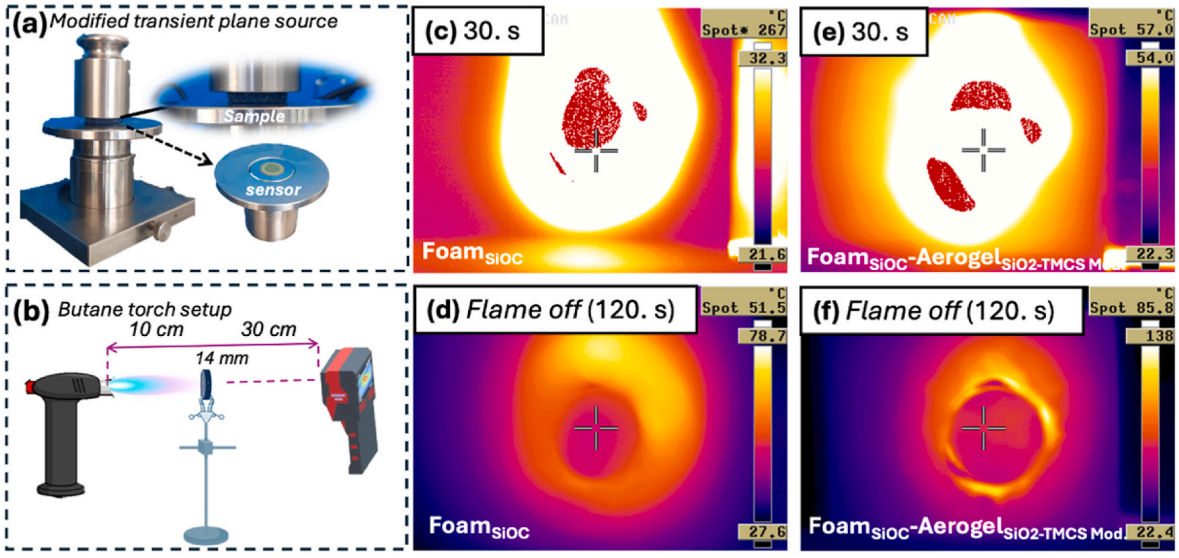

Fig. 7. **(a)** Room-temperature thermal conductivity measurement via MTPS method, **(b)** Illustration of the experimental setup for recording infrared thermal imaging under a butane torch, temperature variation of the backside for **(c)** Foam$_{SiOC}$; at 30 s (spot temp.: 267 °C) **(d)** after the flame was turned off at 120 s (spot temp.: 51 °C), **(e)** Foam$_{SiOC}$-Aerogel$_{SiO2-TMCS\ Mod.}$; at 30 s (spot temp.: 57 °C), and **(f)** after the flame was turned off at 120 s (spot temp.: 85.8 °C).

Among the composites, the Foam$_{SiOC}$-Aerogel$_{SiO2-TMCS\ Mod.}$ provided the best high-temperature insulation, followed by Foam$_{SiOC}$-Aerogel$_{SiO2-SCD}$ (backside temp. of 57.2 °C, Fig. S9a), and Foam$_{SiOC}$-Aerogel$_{SiO2-HMDZ\ Mod.}$ (backside temp. of 123 °C, Fig. S9b).

Fig. 8a displays the experimental setup used to evaluate the thermal insulation performance of SiOC foam-silica aerogel composites under cold conditions. To simulate a cold environment, the samples were placed on dry ice powder (T: −78 °C) in an insulated container. The upper surface temperatures were measured using an infrared camera immediately after placement and again after 5 min of cooling by the dry

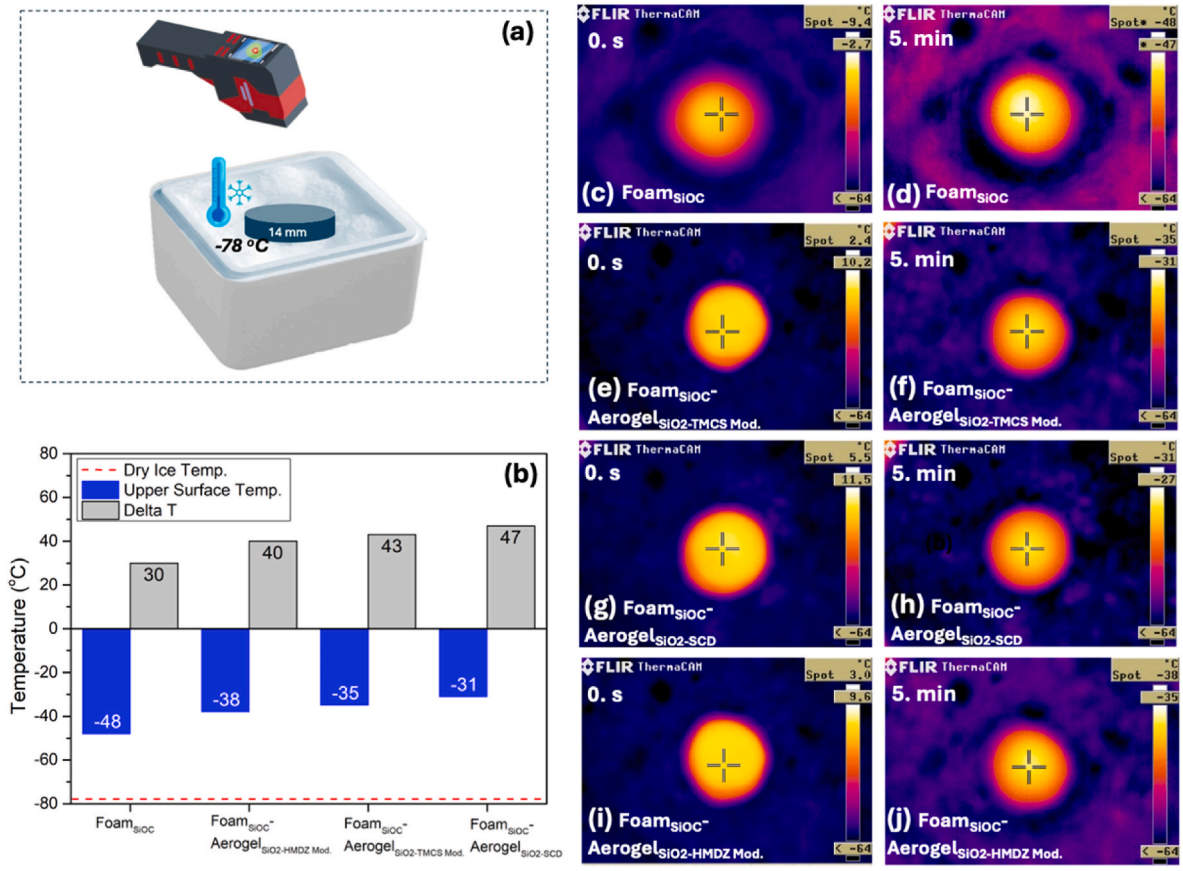

Fig. 8. **(a)** Schematic representation of the dry-ice thermal insulation test, **(b)** the surface temperature of test samples (14 mm thickness) and temperature differences after 5 min contact on dry-ice filled box, thermal infrared images of **(c–d)** Foam$_{SiOC}$ at 0. sec and 5 min, **(e-f)** Foam$_{SiOC}$-Aerogel$_{SiO2-TMCS\ Mod.}$ composite at 0. sec and 5 min, **(g-h)** Foam$_{SiOC}$-Aerogel$_{SiO2-SCD}$ composite at 0. sec and 5 min, and **(i-j)** Foam$_{SiOC}$-Aerogel$_{SiO2-HMDZ\ Mod.}$ composite at 0. sec and 5 min.

ice. The recorded sample's upper surface temperatures and the temperature difference (ΔT) between the cold source and the sample surface are presented in Fig. 8b.

When only SiOC foam was used, the ΔT between the cold side and the sample surface was ~30 °C. In contrast, for silica aerogel-filled foam composites, the ΔT increased to 40 °C, with a maximum ΔT of 47 °C observed for the $Foam_{SiOC}$-$Aerogel_{SiO2\text{-}SCD}$ composite. Fig. 8c–j further illustrate the surface temperature changes of the tested samples after 5 min of contact, as recorded by the infrared thermal camera. Immediately after placement, the upper surface temperature of neat SiOC foam dropped to −9.4 °C (Fig. 8c), whereas the silica aerogel-filled foam composites retained temperatures above 0 °C (Fig. 8e,g,i). After 5 min, the upper surface of the $Foam_{SiOC}$- $Aerogel_{SiO2\text{-}SCD}$ composite only decreased to −31 °C (Fig. 8h), whereas the neat SiOC foam reached as low as −48 °C (Fig. 8d).

It is important to note that no ice formation and accumulations was observed on the composite surfaces even after 5 min of cold exposure. This can be attributed to *i)* The ability of superhydrophobic surfaces to prevent ice formation by extending freezing delay time and inhibiting frosting. In particular, superhydrophobic silica aerogel samples already tested for anti-frosting and anti-icing [44,45], and *ii)* Hierarchical porous structures that generate numerous air pockets between the solid surface and liquid/ice, thereby reducing contact area, adhesion, and thermal conduction at low temperatures. This reduction minimizes heat transfer and further enhances anti-icing performance [46,47]. These findings highlight that the foam-aerogel composites exhibit significantly better thermal insulation performance compared to neat SiOC foam.

4. Conclusions

In conclusion, monolithic SiOC foam-silica aerogel composites were successfully fabricated by filling the open cells of ceramic foam with silica aerogel. The study revealed that both the drying techniques (ambient pressure and CO_2 supercritical drying) and surface modification agents (TMCS and HMDZ) had a significant impact on the structural, morphological, and thermal properties of the composites. The use of TMCS modification agent with ambient pressure drying was particularly effective in achieving fully filled foam cells, resulting in composites with excellent thermal insulation performance. The composites exhibited specific surface areas reaching 440 $m^2\ g^{-1}$ and a consistent total porosity of ~93 vol%. Surface modifications imparted hydrophobicity, with a water contact angle of 133°, while thermal conductivity values remained low at 38 $mW{\cdot}m^{-1}{\cdot}K^{-1}$ at room temperature. The composites showed remarkable thermal management capabilities. For instance, they maintained a surface temperature of 64 °C after 30 min at a heat source of 200 °C, and a temperature of -27 °C for 5 min when subjected to a cold source at -78 °C. Additionally, under direct exposure to a butane flame (~1200 °C), the backside temperature of the composites was only ~57 °C after 30 s. These findings highlight the potential of SiOC foam-silica aerogel composites as highly effective thermal protective materials for use in both hot and cold environments, offering a robust solution for advanced thermal insulation applications.

CRediT authorship contribution statement

Oyku Icin: Writing – review & editing, Writing – original draft, Methodology, Investigation, Data curation, Conceptualization. **Cekdar Vakifahmetoglu:** Writing – review & editing, Supervision, Funding acquisition, Conceptualization.

Funding

This study was funded by TUBITAK (The Scientific and Technological Research Council of Turkey) (grant number: 122M533) and AFOSR (Air Force Office of Scientific Research) (grant number: FA9550-21-1-0279).

Declaration of competing interest

The authors declare that they have no known competing financial interests or personal relationships that could have appeared to influence the work reported in this paper.

Acknowledgments

This study was supported by the Scientific and Technological Research Council of Turkey (TUBITAK) under Grant number 122M533. The authors thank TUBITAK for their support. We recognize the Izmir Institute of Technology, and the Center for Materials Research for the N_2 sorption data analyses, XRD, and SEM investigations. The authors thank Dr. Saadet Güler from the Izmir Katip Çelebi University, Turkiye for the TG-Analysis. Oyku Icin and Cekdar Vakif Ahmetoglu would like to acknowledge the financial support of AFOSR with the program manager, Dr. Ali Sayir, through grant # FA9550-21-1-0279.

Appendix A. Supplementary data

Supplementary data to this article can be found online at https://doi.org/10.1016/j.ceramint.2025.03.167.

References

[1] B.E. Yoldas, M.J. Annen, J. Bostaph, Chemical engineering of aerogel morphology formed under nonsupercritical conditions for thermal insulation, Chem. Mater. 12 (2000) 2475–2484, https://doi.org/10.1021/cm9903428.
[2] C.-Y. Kim, J.-K. Lee, B.-I. Kim, Synthesis and pore analysis of aerogel–glass fiber composites by ambient drying method, Colloids Surfaces A Physicochem. Eng. Asp. 313–314 (2008) 179–182, https://doi.org/10.1016/j.colsurfa.2007.04.090.
[3] L.W. Hrubesh, Aerogel applications, J. Non-Cryst. Solids 225 (1998) 335–342, https://doi.org/10.1016/S0022-3093(98)00135-5.
[4] J.L. Gurav, I.-K. Jung, H.-H. Park, E.S. Kang, D.Y. Nadargi, Silica aerogel: synthesis and applications, J. Nanomater. 2010 (2010), https://doi.org/10.1155/2010/409310.
[5] A.C. Pierre, G.M. Pajonk, Chemistry of aerogels and their applications, Chem. Rev. 102 (2002) 4243–4266, https://doi.org/10.1021/cr0101306.
[6] M.A. Aegerter, N. Leventis, M. Koebel, S.A. Steiner III, Springer Handbook of Aerogels, Springer Nature, 2023.
[7] D. Sivaraman, S. Zhao, S. Iswar, M. Lattuada, W.J. Malfait, Aerogel spring-back correlates with strain recovery: effect of silica concentration and aging, Adv. Eng. Mater. 23 (2021) 2100376, https://doi.org/10.1002/adem.202100376.
[8] S. Iswar, W.J. Malfait, S. Balog, F. Winnefeld, M. Lattuada, M.M. Koebel, Effect of aging on silica aerogel properties, Microporous Mesoporous Mater. 241 (2017) 293–302, https://doi.org/10.1016/j.micromeso.2016.11.037.
[9] W.J. Malfait, H.-P. Ebert, S. Brunner, J. Wernery, S. Galmarini, S. Zhao, G. Reichenauer, The poor reliability of thermal conductivity data in the aerogel literature: a call to action, J. Sol. Gel Sci. Technol. 109 (2024) 569–579, https://doi.org/10.1007/s10971-023-06282-9.
[10] G.M. Pajonk, Some applications of silica aerogels, Colloid Polym. Sci. 281 (2003) 637–651, https://doi.org/10.1007/s00396-002-0814-9.
[11] O. Icin, T. Semerci, G.D. Soraru, C. Vakifahmetoglu, Design and performance comparison of polymer-derived ceramic ambigels and aerogels, ACS Omega (2023), https://doi.org/10.1021/acsomega.3c04607.
[12] H. Hu, J. Wang, C. Li, L. Li, Reinforcement strategies to improve the mechanical properties of nanofibrous aerogels: a review, ACS Appl. Nano Mater. 7 (2024) 26546–26578, https://doi.org/10.1021/acsanm.4c03465.
[13] X. Ye, Z. Chen, S. Ai, B. Hou, J. Zhang, Q. Zhou, F. Wang, H. Liu, S. Cui, Microstructure characterization and thermal performance of reticulated SiC skeleton reinforced silica aerogel composites, Composites, Part B 177 (2019) 107409, https://doi.org/10.1016/j.compositesb.2019.107409.
[14] K.E. Parmenter, F. Milstein, Mechanical properties of silica aerogels, J. Non-Cryst. Solids 223 (1998) 179–189, https://doi.org/10.1016/S0022-3093(97)00430-4.
[15] J. Lin, G. Li, W. Liu, R. Qiu, H. Wei, K. Zong, X. Cai, A review of recent progress on the silica aerogel monoliths: synthesis, reinforcement, and applications, J. Mater. Sci. 56 (2021) 10812–10833, https://doi.org/10.1007/s10853-021-05997-w.
[16] B. Merillas, A. Lamy-Mendes, F. Villafañe, L. Durães, M.Á. Rodríguez-Pérez, Polyurethane foam scaffold for silica aerogels: effect of cell size on the mechanical properties and thermal insulation, Mater. Today Chem. 26 (2022) 101257.
[17] B. Merillas, A. Lamy-Mendes, F. Villafañe, L. Durães, M.Á. Rodríguez-Pérez, Silica-based aerogel composites reinforced with reticulated polyurethane foams: thermal and mechanical properties, Gels 8 (2022) 392.
[18] B. Merillas, F. Villafañe, M.Á. Rodríguez-Pérez, Improving the insulating capacity of polyurethane foams through polyurethane aerogel inclusion: from insulation to superinsulation, Nanomaterials 12 (2022) 2232.
[19] P.K. Renjith, C. Sarathchandran, V. Sivanandan Achary, N. Chandramohanakumar, V. Sekkar, Micro-cellular polymer foam supported silica aerogel: eco-friendly tool

for petroleum oil spill cleanup, J. Hazard Mater. 415 (2021) 125548, https://doi.org/10.1016/j.jhazmat.2021.125548.
[20] H. Xie, W. Yang, A.C.Y. Yuen, C. Xie, J. Xie, H. Lu, G.H. Yeoh, Study on flame retarded flexible polyurethane foam/alumina aerogel composites with improved fire safety, Chem. Eng. J. 311 (2017) 310–317, https://doi.org/10.1016/j.cej.2016.11.110.
[21] B.S. Kim, J. Choi, Y.S. Park, Y. Qian, S.E. Shim, Semi-rigid polyurethane foam and polymethylsilsesquioxane aerogel composite for thermal insulation and sound absorption, Macromol. Res. 30 (2022) 245–253, https://doi.org/10.1007/s13233-022-0026-8.
[22] M. Fashandi, Z. Ben Rejeb, H.E. Naguib, C.B. Park, Ambient pressure dried silica aerogel – melamine foam composite with superhydrophobic, self-cleaning and water remediation properties, Sep. Purif. Technol. 325 (2023) 124201, https://doi.org/10.1016/j.seppur.2023.124201.
[23] M. Fashandi, Z. Ben Rejeb, H.E. Naguib, C.B. Park, Melamine network as a solution for significant enhancement of the mechanical, adsorptive, and surface properties in a novel carbon nanomaterial–silica aerogel composite, ACS Appl. Mater. Interfaces 16 (2024) 23997–24009, https://doi.org/10.1021/acsami.4c00415.
[24] B. Santhosh, C. Vakifahmetoglu, E. Ionescu, A. Reitz, B. Albert, G.D. Soraru, Processing and thermal characterization of polymer derived SiCN (O) and SiOC reticulated foams, Ceram. Int. 46 (2020) 5594–5601.
[25] A. Zambotti, E. Ionescu, N. Gargiulo, D. Caputo, C. Vakifahmetoglu, B. Santhosh, M. Biesuz, G.D. Sorarù, Processing of polymer-derived, aerogel-filled, SiC foams for high-temperature insulation, J. Am. Ceram. Soc. 106 (2023) 4891–4901, https://doi.org/10.1111/jace.19118.
[26] J. Feng, Z. Ma, J. Wu, Z. Zhou, Z. Liu, B. Hou, W. Zheng, S. Huo, Y.-T. Pan, M. Hong, Q. Gao, Z. Sun, H. Wang, P. Song, Fire-safe aerogels and foams for thermal insulation: from materials to properties, Adv. Mater. n/a (2024) 2411856, https://doi.org/10.1002/adma.202411856.
[27] C. Sugie, A. Navrotsky, S. Lauterbach, H.-J. Kleebe, G. Mera, Structure and thermodynamics of silicon oxycarbide polymer-derived ceramics with and without mixed-bonding, Materials 14 (2021), https://doi.org/10.3390/ma14154075.
[28] O. Icin, A.M. Abebe, G.D. Soraru, C. Vakifahmetoglu, SiOC foam-aerogel composites: optimal balance of lightness and excellent thermal insulation, J. Am. Ceram. Soc. 107 (2024) 6729–6740, https://doi.org/10.1111/jace.19967.
[29] O. Icin, C. Vakifahmetoglu, Dye removal by polymer derived ceramic nanobeads, Ceram. Int. 47 (2021) 27050–27057, https://doi.org/10.1016/j.ceramint.2021.06.118.
[30] A. Ayral, J. Phalippou, T. Woignier, Skeletal density of silica aerogels determined by helium pycnometry, J. Mater. Sci. 27 (1992) 1166–1170, https://doi.org/10.1007/BF01142014.
[31] J. Wang, D. Petit, S. Ren, Transparent thermal insulation silica aerogels, Nanoscale Adv. 2 (2020) 5504–5515.
[32] F. Zemke, J. Gonthier, E. Scoppola, U. Simon, M.F. Bekheet, W. Wagermaier, A. Gurlo, Origin of the springback effect in ambient-pressure-dried silica aerogels: the effect of surface silylation, Gels 9 (2023) 160.
[33] R. Su, X. Wang, D. Wang, L. Li, G. Liang, Z. Zheng, K. Li, Preparation of carbon foam-reinforced carbon aerogels and their copyrolysis mechanism, Microporous Mesoporous Mater. 319 (2021) 111059, https://doi.org/10.1016/j.micromeso.2021.111059.
[34] W. Guo, O. Icin, C. Vakifahmetoglu, D. Kober, A. Gurlo, M.F. Bekheet, Magnesium ion battery anode from polymer-derived SiOC nanobeads, Adv. Funct. Mater. 33 (2023) 2304933, https://doi.org/10.1002/adfm.202304933.
[35] F. Zemke, E. Scoppola, U. Simon, M.F. Bekheet, W. Wagermaier, A. Gurlo, Springback effect and structural features during the drying of silica aerogels tracked by in-situ synchrotron X-ray scattering, Sci. Rep. 12 (2022) 7537, https://doi.org/10.1038/s41598-022-11127-6.
[36] D. Huang, C. Guo, M. Zhang, L. Shi, Characteristics of nanoporous silica aerogel under high temperature from 950°C to 1200°C, Mater. Des. 129 (2017) 82–90, https://doi.org/10.1016/j.matdes.2017.05.024.
[37] J.M. Kim, S.M. Chang, S.M. Kong, K.-S. Kim, J. Kim, W.-S. Kim, Control of hydroxyl group content in silica particle synthesized by the sol-precipitation process, Ceram. Int. 35 (2009) 1015–1019, https://doi.org/10.1016/j.ceramint.2008.04.011.
[38] M. V Khedkar, S.B. Somvanshi, A. V Humbe, K.M. Jadhav, Surface modified sodium silicate based superhydrophobic silica aerogels prepared via ambient pressure drying process, J. Non-Cryst. Solids 511 (2019) 140–146.
[39] Z. Song, Y. Zhao, M. Yuan, L. Huang, M. Yuan, S. Cui, Thermal insulation and moisture resistance of high-performance silicon aerogel composite foam ceramic and foam glass, Adv. Eng. Mater. 24 (2022) 2101508, https://doi.org/10.1002/adem.202101508.
[40] R.B. Torres, J.P. Vareda, A. Lamy-Mendes, L. Durães, Effect of different silylation agents on the properties of ambient pressure dried and supercritically dried vinyl-modified silica aerogels, J. Supercrit. Fluids 147 (2019) 81–89.
[41] S.-W. Hwang, T.-Y. Kim, S.-H. Hyun, Effect of surface modification conditions on the synthesis of mesoporous crack-free silica aerogel monoliths from waterglass via ambient-drying, Microporous Mesoporous Mater. 130 (2010) 295–302, https://doi.org/10.1016/j.micromeso.2009.11.024.
[42] P.M. Shewale, A.V. Rao, A.P. Rao, Effect of different trimethyl silylating agents on the hydrophobic and physical properties of silica aerogels, Appl. Surf. Sci. 254 (2008) 6902–6907, https://doi.org/10.1016/j.apsusc.2008.04.109.
[43] A.S. E1461-13, Standard Test Method for Thermal Diffusivity by the Flash Method, 2022.
[44] Y. Xiong, Z. Zhang, Y. Liu, M. Ye, C. Hu, J. Chen, H. Yan, Y. Huang, Loading of aerogels in self-healable polyurea foam to prepare superhydrophobic tough coating with ultra-long freezing delay time and high durability, Surf. Interfaces 51 (2024) 104763, https://doi.org/10.1016/j.surfin.2024.104763.
[45] Z. Zhang, L. A, H. Hu, X. Bai, H. Hu, An experimental study on the detrimental effects of deicing fluids on the performance of icephobic coatings for aircraft icing mitigation, Aero. Sci. Technol. 119 (2021) 107090, https://doi.org/10.1016/j.ast.2021.107090.
[46] C. Wu, H. Geng, S. Tan, J. Lv, H. Wang, Z. He, J. Wang, Highly efficient solar anti-icing/deicing via a hierarchical structured surface, Mater. Horiz. 7 (2020) 2097–2104.
[47] Y. Zhang, X. Fan, X. Li, Z. Zhang, Y. Zhang, Z. Chen, S. Ge, Y. Wang, M. Zhu, Microstructure design of black ceramic composite surface towards photothermal superhydrophobic anti-icing, Chem. Eng. J. 498 (2024) 155101, https://doi.org/10.1016/j.cej.2024.155101.